

Signs of strong Na and K absorption in the transmission spectrum of WASP-103b

M. Lendl, P. E. Cubillos, J. Hagelberg, A. Müller, I. Juvan, L. Fossati

▶ **To cite this version:**

M. Lendl, P. E. Cubillos, J. Hagelberg, A. Müller, I. Juvan, et al.. Signs of strong Na and K absorption in the transmission spectrum of WASP-103b. Astronomy and Astrophysics - A&A, 2017, 606, 10.1051/0004-6361/201731242 . insu-03692483

HAL Id: insu-03692483

https://insu.hal.science/insu-03692483

Submitted on 10 Jun 2022

HAL is a multi-disciplinary open access archive for the deposit and dissemination of scientific research documents, whether they are published or not. The documents may come from teaching and research institutions in France or abroad, or from public or private research centers.

L'archive ouverte pluridisciplinaire **HAL**, est destinée au dépôt et à la diffusion de documents scientifiques de niveau recherche, publiés ou non, émanant des établissements d'enseignement et de recherche français ou étrangers, des laboratoires publics ou privés.

A&A 606, A18 (2017)
DOI: 10.1051/0004-6361/201731242
© ESO 2017

Astronomy & Astrophysics

Signs of strong Na and K absorption in the transmission spectrum of WASP-103b⋆

M. Lendl[1,2], P. E. Cubillos[1], J. Hagelberg[3,4], A. Müller[2], I. Juvan[1,5], and L. Fossati[1]

[1] Space Research Institute, Austrian Academy of Sciences, Schmiedlstr. 6, 8042 Graz, Austria
e-mail: monika.lendl@oeaw.ac.at
[2] Max Planck Institute for Astronomy, Königstuhl 17, 69117 Heidelberg, Germany
[3] Institut de Planétologie et d'Astrophysique de Grenoble, Université Grenoble Alpes, CS 40700, 38058 Grenoble Cedex 9, France
[4] University of Hawaii, 2680 Woodlawn Dr., Honolulu, HI 96822, USA
[5] Institut für Geophysik, Astrophysik und Meteorologie, Karl-Franzens-Universität, Universitätsplatz 5, 8010 Graz, Austria

Received 24 May 2017 / Accepted 15 August 2017

ABSTRACT

Context. Transmission spectroscopy has become a prominent tool for characterizing the atmospheric properties on close-in transiting planets. Recent observations have revealed a remarkable diversity in exoplanet spectra, which show absorption signatures of Na, K and H_2O, in some cases partially or fully attenuated by atmospheric aerosols. Aerosols (clouds and hazes) themselves have been detected in the transmission spectra of several planets thanks to wavelength-dependent slopes caused by the particles' scattering properties.
Aims. We present an optical 550–960 nm transmission spectrum of the extremely irradiated hot Jupiter WASP-103b, one of the hottest (2500 K) and most massive (1.5 M_J) planets yet to be studied with this technique. WASP-103b orbits its star at a separation of less than 1.2 times the Roche limit and is predicted to be strongly tidally distorted.
Methods. We have used Gemini/GMOS to obtain multi-object spectroscopy throughout three transits of WASP-103b. We used relative spectrophotometry and bin sizes between 20 and 2 nm to infer the planet's transmission spectrum.
Results. We find that WASP-103b shows increased absorption in the cores of the alkali (Na, K) line features. We do not confirm the presence of any strong scattering slope as previously suggested, pointing towards a clear atmosphere for the highly irradiated, massive exoplanet WASP-103b. We constrain the upper boundary of any potential cloud deck to reside at pressure levels above 0.01 bar. This finding is in line with previous studies on cloud occurrence on exoplanets which find that clouds dominate the transmission spectra of cool, low surface gravity planets while hot, high surface gravity planets are either cloud-free, or possess clouds located below the altitudes probed by transmission spectra.

Key words. planets and satellites: atmospheres – planets and satellites: gaseous planets – methods: observational – techniques: spectroscopic

1. Introduction

Due to their high temperatures and extended atmospheres, hot Jupiters (i.e., gas giants at orbital periods of a few days) are ideal laboratories for studying the properties of exoplanet atmospheres. Transmission spectroscopy probes the planetary atmosphere's composition and structure by measuring the spectrally resolved absorption during transit. A growing sample of hot-Jupiter transmission spectra from ground and space is revealing a remarkable diversity in spectral signatures. Some planets show prominent absorption signatures of alkali (Na, K), and water (e.g., Charbonneau et al. 2002; Deming et al. 2013; Nikolov et al. 2016; Sedaghati et al. 2016). Many objects however show attenuated features (e.g., Chen et al. 2017; Sing et al. 2015, 2016), and in some the elemental or molecular absorptions are entirely absent at low spectral resolution (Pont et al. 2008; Lendl et al. 2016). Several planets show pronounced slopes of increasing absorption towards shorter wavelengths, as can be explained by scattering on aerosols with small particle sizes (clouds and hazes) lifted to high altitudes in the planetary atmospheres. The level of observed attenuation of the absorption features depends on the particles' abundance, size and atmospheric altitude. The observed slopes stem from scattering on small aerosoles and the slope extension and amplitude depends on the atmospheric temperature and the size distribution of the scattering particles (Lecavelier Des Etangs et al. 2008a).

The relation between planetary characteristics and the occurrence and properties of aerosols is yet to be definitely understood. Stevenson (2016) and Heng (2016) propose that planets with hot atmospheres posses less pronounced cloud features, Stevenson (2016) also suggests that clouds are more common for low surface gravity planets.

In this work, we present the transmission spectrum of one of the most irradiated transiting hot Jupiters known to date, WASP-103b (Gillon et al. 2014). WASP-103b stands out due to its short orbital period of 0.9 d, which is far below the peak of the hot Jupiter period distribution of about three days (e.g., Udry et al. 2003). Due to tidal dissipation of orbital energy, most hot Jupiters are suffering from orbital decay and are spiraling into their host stars (e.g., Matsumura et al. 2010; Patra et al. 2017). WASP-103b is a hot Jupiter in its final stages of orbital decay. Currently, the planetary orbital separation from the

⋆ The spectrophotometric time series data are only available at the CDS via anonymous ftp to cdsarc.u-strasbg.fr (130.79.128.5) or via http://cdsarc.u-strasbg.fr/viz-bin/qcat?J/A+A/606/A18

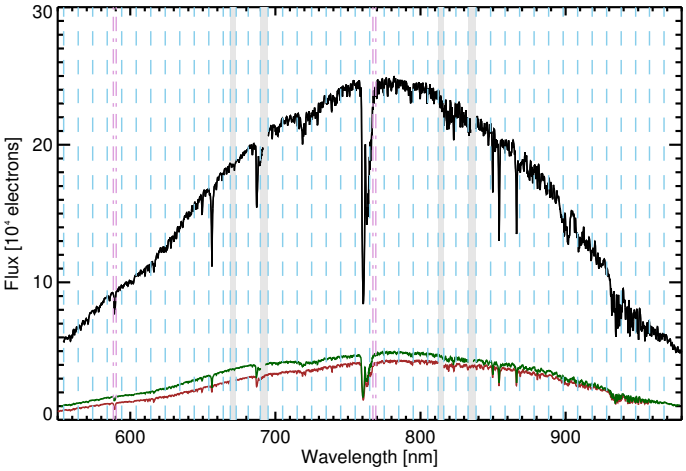


Fig. 1. Average spectra of target (*top*, black) and two reference stars. The 10 nm bins used for spectrophotometric extraction are indicated with blue dashed lines, while the purple dash-dotted lines indicate 5 nm bins centered on the Na and K features. Gaps between the GMOS detectors are shaded in gray.

host star amounts to only 1.16 times its Roche limit, leading to large tidal distortion of the planet (Budaj 2011; Leconte et al. 2011). This fact, paired with the planet's extremely high stellar irradiation makes this object prone to enhanced mass loss (Lammer et al. 2003; Vidal-Madjar et al. 2003).

We describe our GMOS observations in Sect. 2, and detail our analysis approach, and the correction of our measurements for contamination from a nearby star in Sect. 3. In Sect. 4, we present and discuss our results for WASP-103b, before concluding in Sect. 5.

2. Observations and data reduction

2.1. GMOS-North observations

We observed WASP-103 throughout three full transits with GMOS at Gemini North during the nights of 27 June 2015, 10 July 2015, and 03 May 2016 (all UT, program numbers GN-2015A-Q-63 and GN-2016A-Q-26, PI: Hagelberg). All observations were carried out in multi-object spectroscopy mode using the R400 grism and order separation filter OG515. We used custom-cut masks to place slits on the target and two reference stars. The slit width was set to 10 arcsec for all stars to avoid slit losses due to guiding inaccuracies or seeing variations, and the slit length was set to 40 arcsec for the target and the brighter reference to allow for a good sky determination. For the fainter reference, the slit needed to be kept shorter (25 arcsec) to avoid contamination from a nearby star.

Spectral coverage of the target and the brighter reference star is between 550 and 980 nm (top and middle spectra in Fig. 1), while spectra of the fainter reference star (bottom spectrum in in Fig. 1) are slightly offset and cover 530 to 960 nm. Two amplifiers were used to read each of the three CCDs in 1×1 binning and "Slow read" mode. We used custom regions of interest (ROI) to window the detectors and read only the detector areas containing data. Sky conditions were clear throughout all three observations, however, the observations on 10 July 2015 were interrupted for approx. 22 min due to high ambient humidity. We used exposure times of 240 s on 27 June 2015 and 10 July 2015, and exposure times of 180 s on 03 May 2016.

2.2. Spectral extraction and wavelength calibration

We carried out the standard calibrations using the GMOS IRAF routines, and also used these routines to calculate an initial wavelength calibration based on (CuAr) arc frames. The spectra have a pixel scale of 0.68 Å per pixel in the dispersion direction, and a spectral resolution of $R \sim 1200$. Cosmic rays were removed using the LA-cosmic routines (van Dokkum 2001). The resulting 2D spectra were analyzed using custom-built IDL routines. To correct the spectra for the sky background, we selected two regions well above and below the stellar spectrum in the spatial direction. For each spatial pixel, we fitted a linear trend to the flux values in these regions, determined the sky below the stellar spectrum via interpolation, and subtracted it. This procedure serves to remove any background trends of instrumental or physical origin, however for the data described here, no appreciable trends were seen across the sky background in the spatial direction. After sky removal, the spectra were extracted by summing flux inside large (18 px) apertures.

Visual inspection of the derived spectra quickly revealed residual wavelength offsets of up to 0.5 nm, between target and reference stars, and wavelength drifts up to 0.3 nm, affecting the spectra of individual stars throughout each observing sequence. As our smallest wavelength bin is 2 nm, these drifts are large enough to affect our results and we thus refined the wavelength solution on the target and reference spectra as follows before proceeding. To calculate a correct wavelength solution for all images, we first removed telluric features with the molecfit routines (Smette et al. 2015; Kausch et al. 2015). We then calculated improved wavelength solutions based on these corrected spectra and applied these to the individual (uncorrected) spectra before extracting spectrophotometry. The improved wavelength solutions were found in a three-step process: first, we identified the best frames of each sequence as reference images and, for each star, shifted all other spectra obtained during the same night to the wavelength solution of these reference spectra. We did this by cross-correlating a set of reference regions and, based on the inferred wavelength shifts, adapted the wavelength solution of each of the three detectors separately. Once all spectra of each sequence and star were aligned to the respective reference spectrum, we proceeded to finding an improved wavelength solution. To do so, we first combined all spectra of each star and date, producing a higher S/N spectrum. We then refined the wavelength solution of the target spectrum as follows. We fitted the continuum, normalized the target spectrum and cross-correlated a set of well-resolved features against a PHOENIX (Husser et al. 2013) model spectrum of an $T_{\rm eff} = 6100$ K, $\log g = 4.50$ solar-metallicity star that had been normalized and convolved down to the resolution of our data. Again, the wavelength solution was corrected by fitting cross-correlating a set of reference regions. Following the same procedure, we finally matched the two reference star spectra to that of the target.

Once we were certain of a reliable wavelength calibration, we binned the spectra of target and reference stars in 10 and 20 nm wide wavelength bins and created relative transit light curves for each bin. To reach a higher wavelength resolution on the Na and K features, we add 2, 5 and 10 nm bins centered on these features. We find that the most precise light curves are obtained when only the fainter reference star is used instead of the sum of both references, since the brighter reference star showed strong correlated noise. See Figs. 3 and 4 for these spectrophotometric light curves, together with the best models described below.

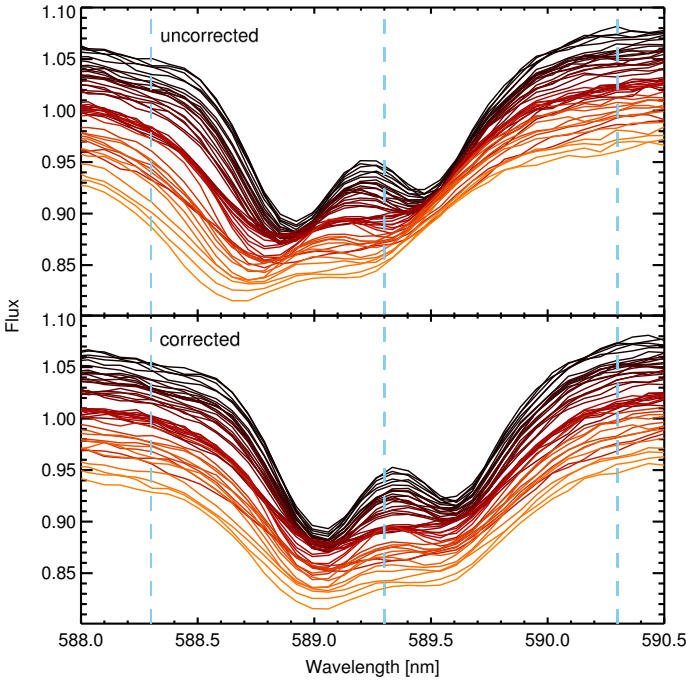


Fig. 2. Enlargement of the Na feature at 589 nm showing all spectra obtained on 07 June 2015. Flux is given in arbitrary units, and the spectra are color-coded and shifted on the y-axis for illustrative purposes. The *top panel* shows the drift of the wavelength solution throughout the sequence before wavelength recalibration, and the *bottom panel* shows the same sequence of spectra after recalibration. Vertical blue dashed lines indicate the center and limits of our smallest wavelength bin around the Na feature.

3. Lightcurve analysis

3.1. Fitting method

Our code uses a differential evolution Markov chain Monte Carlo (DEMCMC) approach for the combined analysis of transit lightcurves, combining the publicly available parallelized MC3 code (Cubillos et al. 2017)[1] with the prescription for transit lightcurve shape by Mandel & Agol (2002). Depending on the available resources (differential evolution MCMC methods rely on a large number of chains run in parallel), the sampling algorithm may be set to either a Metropolis-Hastings algorithm (e.g. Carlin & Louis 2009), a DEMCMC (ter Braak 2006) algorithm, or the DEMC-z algorithm with snooker proposals (ter Braak & Vrugt 2008). Convergence is checked via the Gelman-Rubin (Gelman & Rubin 1992) test.

To account for photometric variations stemming from instrumental, atmospheric or stellar effects, our code includes photometric baseline models, parametrizations of external variables such as time, stellar FWHM, and sky background. The parametric baseline coefficients can either be included as jump parameters or calculated via least-square minimization at each MCMC step (following Gillon et al. 2010). The later option can be advantageous for computational reasons as it reduces the number of jump parameters, however the first option allows to visualize any correlations between photometric baseline parameters and inferred transit parameters. We assume a minimal baseline model assuming a second-order time polynomial, and accept more complicated models only if the Bayes factor (e.g., Schwarz 1978) estimated from the Bayesian Information Criterion indicated significantly higher probability. It is also possible to include a common prescription of correlated noise for spectrophotometric light curves from the same epoch and instrument based on the common noise model (CNM) described in Lendl et al. (2016). Before launching the MCMC, we run a least-squares minimization and estimate the amplitudes of additional white and red noise in each of the lightcurves via the β_r and β_w factors. β_w is defined as the ratio of the residual RMS to the mean error and β_r is calculated by comparing the residual RMS of the binned to the residuals of the unbinned data set (Winn et al. 2008; Gillon et al. 2010). For each lightcurve, we then rescale the errors by multiplying them with the product $CF = \beta_w \times \beta_w$. This procedure also assures the correct weighting between several data sets of unequal quality.

The following parameters can be set as fitted ("jump") parameters in the analysis:

- the star to planet radius ratio $\frac{R_p}{R_*}$;
- the impact parameter, b;
- the transit duration, T_{14};
- the time of mid-transit, T_0;
- the orbital period, P;
- $\sqrt{e}\sin\omega$ and $\sqrt{e}\cos\omega$, where e is the orbital eccentricity and ω is the argument of periastron;
- the linear combination of the quadratic limb-darkening coefficients (u_1, u_2) in each wavelength band, $c_{1,i} = 2u_{1,i} + u_{2,i}$ and $c_{2,i} = u_{1,i} - 2u_{2,i}$ (Holman et al. 2006);
- offsets $\left(\Delta\frac{R_p}{R_*}\right)_i$ from a reference radius ratio $\left(\frac{R_p}{R_*}\right)_0$ for each wavelength channel. $\left(\frac{R_p}{R_*}\right)_0$ is usually determined from broadband photometry or "white"-light analysis binning all spectrophotometric data together. It is not possible to fit $\left(\Delta\frac{R_p}{R_*}\right)_i$ and $\frac{R_p}{R_*}$ simultaneously;
- the coefficients of the photometric baseline models.

3.2. WASP-103 analysis

For the analysis of the GMOS WASP-103 data, we used the DEMCMC algorithm running between 30 and 180 parallel (depending on the number of fitted light curves) chains of 20 000 points each. To calculate limb darkening coefficients for all our wavelength channels, we used the routines by Espinoza & Jordán (2015) together with the response function for the GMOS R400 grism[2]. We calculated coefficients for a $T_{\rm eff} = 6110.0$ K, M/H = 0.00 and $v_{\rm turb} = 2.0$ km s^{-1} star for surface gravities of $\log g = 4.0$ and $\log g = 4.5$ using interpolated PHOENIX models (option P100). We then interpolated these values to match the surface gravity of WASP-103, $\log g = 4.22$. We kept the limb-darkening values fixed during our analysis. We verified that this did not impact our results by performing an additional run while letting the limb darkening parameters vary, assuming only a wide (width 0.1, much larger than the variation of the parameters between neighboring wavelength bins) Gaussian prior centered on the model values. Results from this test were near-identical to those of with fixed limb-darkening parameters.

3.2.1. Contamination

WASP-103 was identified to possess a nearby (0.24") star by Wöllert & Brandner (2015), which is blended with WASP-103

[1] https://github.com/pcubillos/MCcubed

[2] Available at https://www.gemini.edu/sciops/instruments/gmos/spectroscopy-overview/gratings

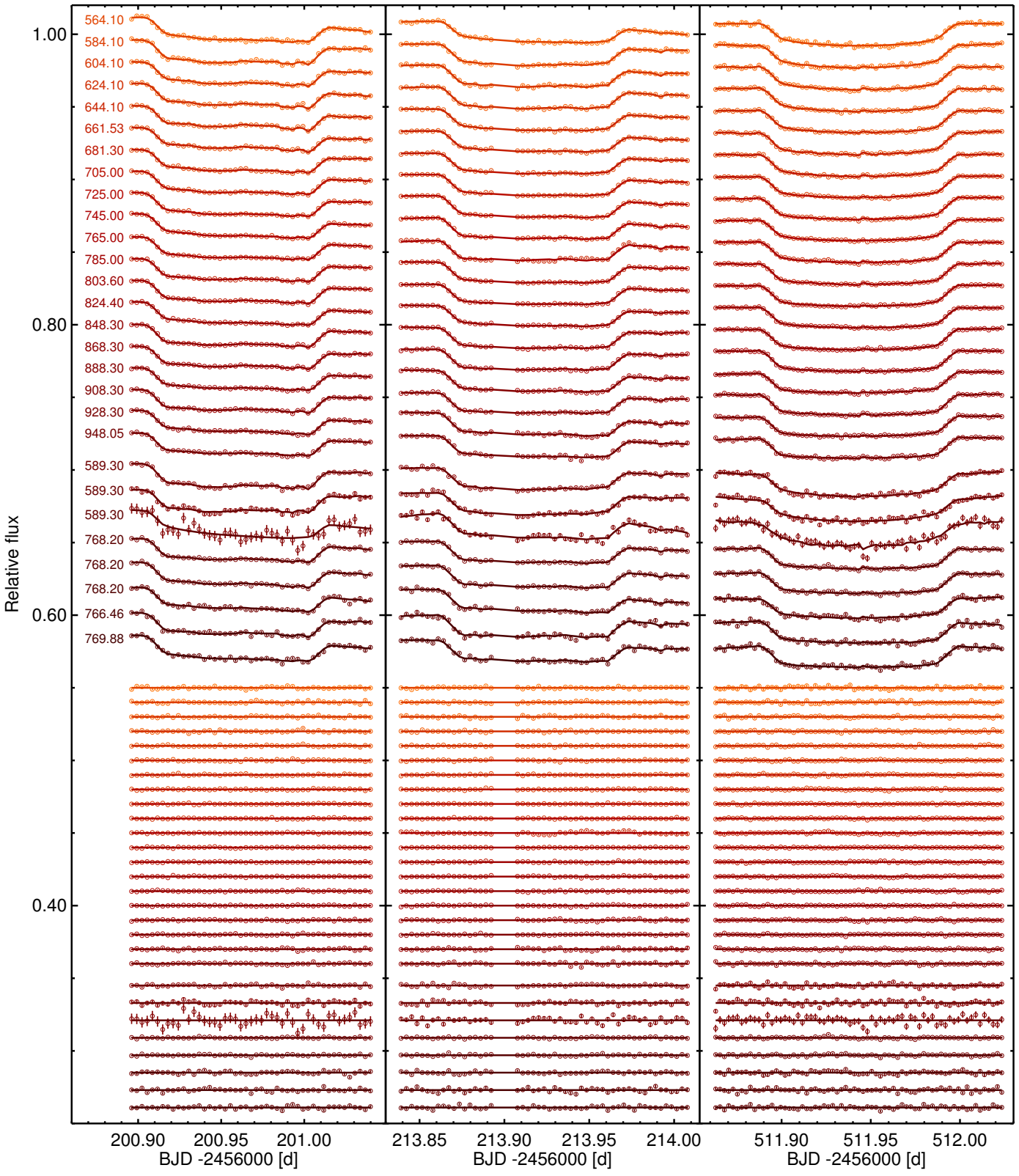


Fig. 3. Spectrophotometric light curves of the three observation epochs (*left, center, and right panels*) obtained using 20 nm bins, as well as bins centered on the Na and K line features. The central wavelength of each bin (in nm) is indicated in the left panel. The light curves centerend on the alkali features are ordered by bin width (*from top to bottom*): 10, 5 and 2 nm. Residuals are shown below, in the same order as the light curves.

in our data. Further observations by Ngo et al. (2016) and Cartier et al. (2017) reveal this contaminant to be a $T = 4400 \pm 200$ K K5V star, most likely physically associated to WASP-103 (Cartier et al. 2017). Third light, if unaccounted for, introduces systematic effects in transmission spectra which may be misinterpreted as effects stemming from the planetary atmosphere. To

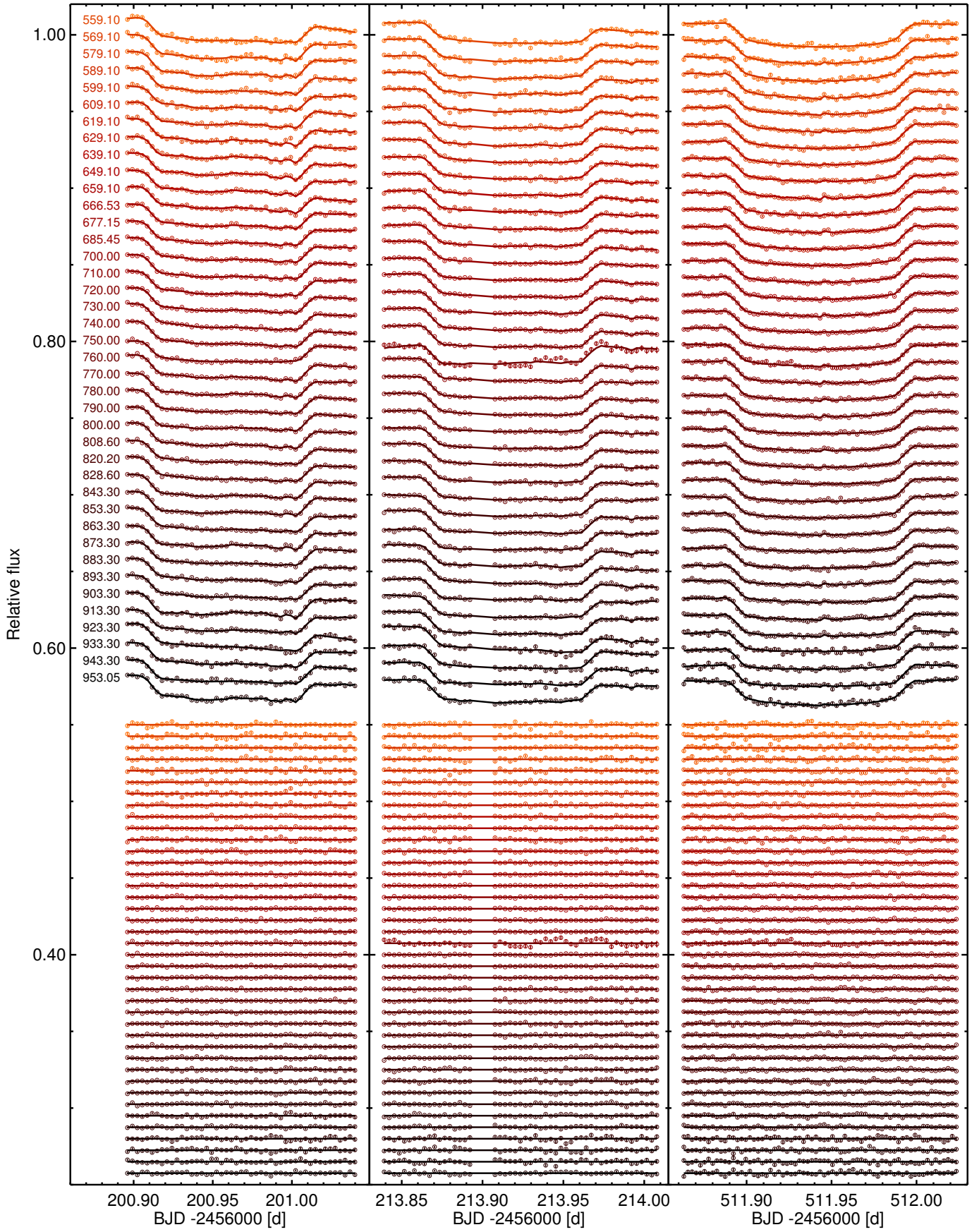


Fig. 4. Spectrophotometric light curves of the three observation epochs (*left, center, and right panels*) obtained using 10 nm bins. The central wavelength of each bin (in nm) is indicated in the *left panel*. Residuals are shown below, in the same order as the light curves.

correct our measurements, we estimate the contaminating flux in the observed wavelength bands using PHOENIX model spectra (Husser et al. 2013) and the target and contaminant properties of Cartier et al. (2017). We binned PHOENIX model spectra to the spectral bins of our transmission spectrum and interpolated them to the target and contaminant parameters. We then calculated the contaminating flux ratio for each wavelength bin i as

$$\left(\frac{F_{\rm cont}}{F_{W103}}\right)_i = \left(\frac{R_{\rm cont}}{R_{W103}}\right)^2 \left(\frac{M_{\rm cont}}{M_{W103}}\right)_i, \quad (1)$$

where $(M_{W103},M_{\rm cont})_i$ are the binned model spectra, and $R_{\rm cont}/R_{W103}$ is the contaminant/target radius ratio. To estimate the uncertainties, we drew 10000 temperature values from Gaussian distributions of target and contaminant values centered on the values given by Cartier et al. (2017), and with a standard deviation of their respective $1-\sigma$ errors. As the radius ratio is not independent of the stellar temperature, it needs to be estimated for each combination of target and contaminant temperatures. We did this by interpolating and binning model spectra for all temperature values and using these together with the measured J, H and K band magnitude ratios of (Cartier et al. 2017) to infer appropriate radius ratios for our sample of target and contaminant temperatures. For this set of 10 000 simulated pairs of spectra and radius ratios, we inferred the resulting flux ratios in the spectral bins of our analysis and estimated the errors on the assumed flux ratios from this distribution. The obtained values and uncertainties are given in Table A.1. These values are in good agreement with those given by Southworth & Evans (2016) and Cartier et al. (2017). We note that errors in the assumed contamination do not affect each spectral measurement independently, but rather cause horizontal shifts of the full transmission spectrum, and/or introduce a wavelength-dependent slope. To evaluate any such effect on our transmission spectrum, we derive the impact of each element of our sample on the measured R_P/R_* values and then infer the 3-σ contours. These contours are shown as dotted lines in Fig. 7, and indicate that, while the measurements may be shifted up or down by 0.0013 in $R_{\rm p}/R_*$, potentially introduced slopes are small.

3.2.2. White light curves

We first performed an independent analysis of each of the white light curves obtained by combining the full spectra of each date. Here, we tested a wide variety of parametric baseline models to find the optimal fit to the observations of each date, selecting a more complicated model over a simple one only if the Bayes factor indicates significantly higher probability. Error bars were not adapted to compensate for red or white noise at this step, as this would bias the inferred BIC values. The observations of 27 June 2015 and 10 July 2015 are best fit by polynomials of second order in time together with a sine function, $f(t) = A_0 + A_1 t + A_2 t^2 + B_0 \sin(B_1 t + B_2)$ (a common behavior for GMOS data, see Stevenson et al. 2014; von Essen et al. 2017), while for the light curve of 03 May 2016, a second order time polynomial is adequate. Using these baseline models, and allowing for error scaling to compensate for excess noise, we infer $R_{\rm p}/R_*$ values of 0.1120 ± 0.0021, 0.1158 ± 0.0011, and 0.1157 ± 0.0007 for the light curves observed on 27 June 2015, 10 July 2015, and 03 May 2016, respectively. These values are in good agreement, with the two latter light curves producing near-identical values and the first light curve, which is also the least precise, showing a marginally smaller value. This is in line with the non-detection of rotational modulation (which would lead to time-variable transit depths) for the host star (Gillon et al. 2014). From a combined fit of all three white light curves, we derive the transit parameters listed in Table 1. Again, these values are in good agreement (<1.5σ difference) with those published by Southworth et al. (2015), Southworth & Evans (2016) and Cartier et al. (2017).

Table 1. Transit parameters inferred from an analysis of the white light curves.

Parameter	Value
Time of mid-transit, T_0 [HJD$_{\rm UTC}$]	7511.943617 ± 0.000076
Star/planet radius ratio, R_P/R_*	$0.11442^{+0.00050}_{-0.00043}$
Impact parameter, b	$0.074^{+0.066}_{-0.048}$
Transit duration, T_{14} [d]	0.11232 ± 0.00019
Period [d]	0.92554705 ± 0.0000004

3.2.3. Inference of the transmission spectrum

We extracted spectrophotometry covering the full spectral range for wavelength intervals of 10 nm and 20 nm width, as well as for 2 nm, 5 nm and 10 nm windows centered on the Na feature. Due to the separation of the K feature components (which is 3.4 nm, compared to 0.6 nm for the Na feature), we placed two 2 nm bins at the center of the two components and one bin between them, in addition to 5 nm and 10 nm bins covering the whole feature. We analyzed the full-range 10 and 20-nm bins as separate sets, each time including the narrow bins centered on Na and K. Instead of fixing the transit shape parameters (T_0, b, and T_{14}) when inferring the transmission spectrum, which may result in under-estimated errors, we let these parameters vary, but imposed normal priors centered on the inferred value and 1-σ errors obtained from the analysis of the white light curves. We used the white $R_{\rm p}/R_*$ values measured above as reference radii used in the calculation of the common noise model and the planetary radius variations $(\Delta R_{\rm p}/R_*)_i$.

We first carried out individual analyses of the transmission spectra obtained at the individual epochs, to search for any variations. For each set, we used the best parametric model found from the analysis of the white light curves (see Sect. 3.2.2), fitting all coefficients of the time polynomial as well as the amplitude of the sine function. We also tested the addition of a common noise model, finding that its addition is warranted by significant BIC improvements for all three dates. Additionally, the resulting transmission spectra obtained when including a common noise model show better agreement between the three epochs. We find that the spectra obtained on the three dates are in reasonable overall agreement with one another (see the upper panel of Fig. 5), with the discrepancy of two measurements in the same wavelength bin at a level of 0.65σ and below 2.3σ in all cases. For the 10 nm bins, agreement is at a similar level, with a median of 0.55σ and individual measurements disagreeing by as much as 2.5σ. The differences are most pronounced at short or long wavelengths, which could indicate that limited signal to noise combined with larger supplementary wavelength corrections as limiting factors.

To find the optimal transmission spectrum based on all available data, we performed a combined analysis of all GMOS data, allowing for a single planetary radius offset $(\Delta R_{\rm p}/R_*)_i$ per wavelength channel. The resulting transmission spectra are shown in Figs. 5 (20 nm bins) and 6 (10 nm bins), and given in Table A.2.

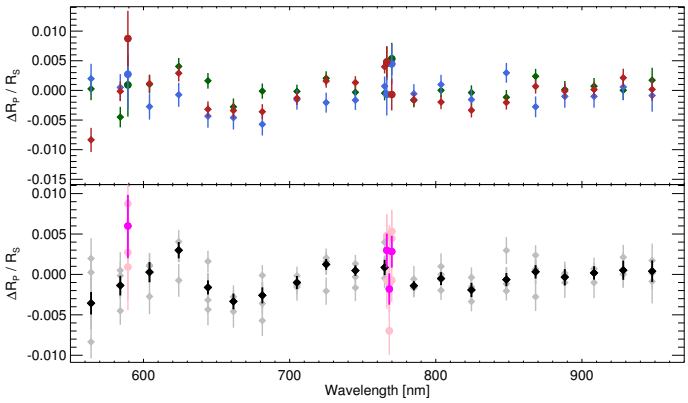


Fig. 5. Inferred R_p/R_* offsets for wavelength bins of using 20 nm width. Top: results from separate analyses to each epoch, where blue, red and green points refer to results from 27 June 2015, 10 July 2015, and 03 May 2016, respectively. Bottom: results from the combined analysis of all data (black points), together with the 2 nm bins centered on the Na and K features. Results from the separate analyses are shown in gray.

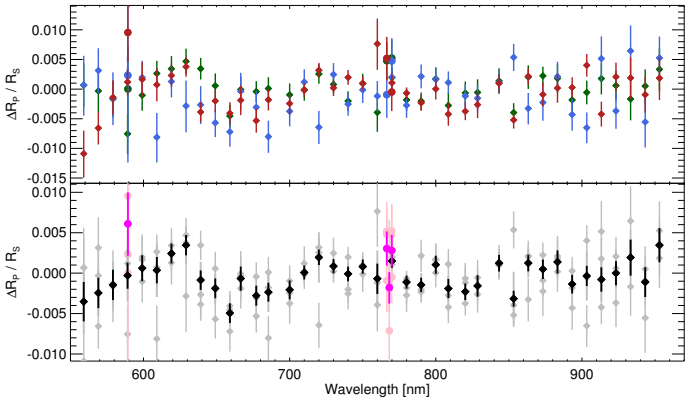


Fig. 6. Inferred R_p/R_* offsets for wavelength bins of using 20 nm width. *Top*: results from separate analyses to each epoch, where blue, red and green points refer to results from 27 June 2015, 10 July 2015, and 03 May 2016, respectively. *Bottom*: results from the combined analysis of all data (black points), together with the 2 nm bins centered on the Na and K features. Results from the separate analyses are shown in gray.

4. Results and discussion

4.1. Model atmospheres

We compute model transmission spectra of WASP-103b, using solar abundances, to aid the interpretation of our observations. To produce atmospheric transmission forward models of WASP-103b, we use the open-source Python Radiative Transfer in a Bayesian framework (Pyrat Bay) package[3] (Cubillos et al., in prep.), which is based on the Bayesian Atmospheric Radiative Transfer package (Blecic 2016; Cubillos 2016). The models of WASP-103b consider molecular opacities for H_2O (HITEMP, Rothman et al. 2010), collision induced absorption from H_2-H_2 (Borysow et al. 2001; Borysow 2002) and H_2-He (Borysow et al. 1988, 1989; Borysow & Frommhold 1989), H_2 Rayleigh scattering (Lecavelier Des Etangs et al. 2008b), and resonant alkali lines (Burrows et al. 2000).

The code computes line-by-line radiative-transfer for a 1D atmospheric model consisting of concentric shell layers, in hydrostatic equilibrium, and thermochemical-equilibrium abundances (Blecic et al. 2016). We assumed isothermal temperature profiles with a temperature of 2500 K, and calculated thermochemical-equilibrium models from solar elemental abundances scaling the metallicities to 0.1, 1, and 10 times the solar value.

[3] http://pcubillos.github.io/pyratbay

4.2. Spectral slope by scattering or contamination

We use our combined transmission spectra to study the atmospheric properties of WASP-103b. Southworth et al. (2015) used broadband light curves to infer the presence of a strong scattering slope in the transmission spectrum of WASP-103b, which holds even after correcting their measurements from contamination by the nearby star (Southworth & Evans 2016). While our data do not span the full extent in wavelength of their measurements, in particular we have no data bluewards of 560 nm, we do not observe any evident trend in the transmission spectrum. To test this, we fitted a straight line with a linear model in wavelength to the 10 nm bin data set, excluding the narrow wavlength bins centered on the Na and K features. We found a negligible slope of absorption increasing with wavelength $1.04 \times 10^{-6} \pm 1.54 \times 10^{-6}$ in R_P/R_* per nm (best values and errors were determined via an MCMC bootstrap approach drawing 10 000 subsamples). Comparing this solution with a straight horizontal line, we find no evidence of the slope producing a significantly more accurate fit to the data (Bayes factor 0.2). We show our measurements next to those of Southworth & Evans (2016) in Fig. 7. Next to the data, we show our best-fit slope as well as a Rayleigh scattering slope inferred from the broadband data as in Southworth & Evans (2016). The latter is parametrized, following Lecavelier Des Etangs et al. (2008a), by $\frac{dR_p/R_*(\lambda)}{d\ln\lambda} = -0.0066(17)$. Additional observations at shorter wavelengths would be helpful to definitely measure any scattering signature in the atmosphere of WASP-103b.

Beside the physical properties of the planetary atmosphere, blended third light from a companion star affects the transmission spectrum of WASP-103b. While we correct for this third light in our analysis, uncertainties in the assumed spectral type of target and contaminating star can lead to residual slopes and overall offsets. As described in Sect. 3.2.1, we have carried out a large set of simulations, perturbing the assumed temperatures of target and contaminant within the errors given by Cartier et al. (2017). We find that even in the most extreme cases, the added slopes are too small to significantly impact the shape of our observed transmission spectrum. However, our transmission spectrum may be subject to an overall offset of ± 0.0013 in R_P/R_*. This is illustrated in Fig. 7, where two dotted gray lines indicate the potentially added slopes (assuming the 3-σ envelop to all simulated cases).

4.3. Na and K absorption features

Absorption by Na and K produces prominent features in planetary transmission spectra. As WASP-103b has a high mass and hence density, the predicted amplitude of these features is small compared to other planets studied previously with ground-based transmission spectroscopy (e.g., 2.7 times smaller than those of the recently-studied WASP-39b, Nikolov et al. 2016, and WASP-17b ,Sedaghati et al. 2016), these features are inherently difficult to detect for WASP-103b. Our data cover both the 590 nm Na and the 766 nm K doublets, and we place a set of narrow bins on these features to test for extra absorption. As shown in Fig. 8, we detect signs of added absorption at the line cores of both features. The Na feature is more clearly detected. Even

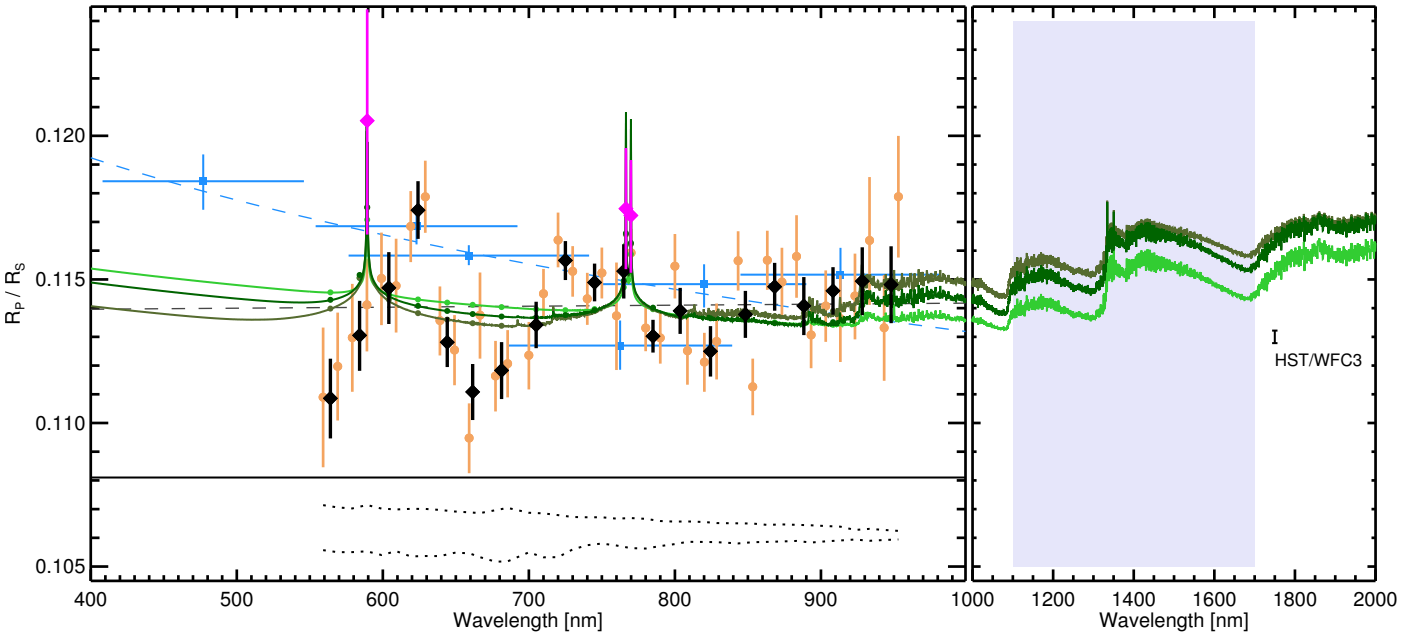


Fig. 7. Optical transmission spectrum of WASP-103b. Measurements obtained with 10 and 20 nm wide bins are shown as brown filled circles and black squares, respectively. Measurements in 2 nm wide bins centered on the Na feature, as well as on both components of the K feature are shown in magenta. Observations by Southworth & Evans (2016) are indicated by blue squares, together with their inferred spectral sloped (blue dashed line). The best-fit spectral slope inferred from our data is shown as a gray dashed line. Model transmision spectra for WASP-103b's are shown as a light green (0.1 × solar metallicity), dark green (solar metallicity) and olive (10 × solar metallicity) lines and filled circles indicate the models binned to the resolution of the data. Below, the two dotted lines indicate the possible added spectral slopes (at 3-σ level) due to uncertainties in the properties of WASP-103b and the contaminating star. The vertical scale is identical to that of the *upper panel*. In the *right panel*, the shaded region indicates the wavelength coverage of HST/WFC3's G141 grism, and the expected precision of spectrophotometric WFC3 measurements is indicated.

though the broadband transmission spectrum shows a trend (of unknown origin) across the 560–630 nm region, the measured absorption is enhanced for the 2 nm bin centered on the Na feature compared to the neighboring points (see Fig. 8). We resolve the two components of the K feature by placing a 2 nm wide bin on each of the two peaks as well as on 2 nm wide bin between them. Further, we place bins of 5 and 10 nm centrally on the feature. Both components show enhanced absorption compared to the neighboring spectral bins, or the spectral bin placed between the two components.

For both features, the absorption appears to be slightly larger (0.74, 0.36 and 0.43σ for the Na and the blue and red components of the K line, respectively) than predicted from our model spectra. Enhanced absorption features could be related to the planet's tidally distorted state, for which we calculate (using the Roche lobe model by Budaj 2011, as well as stellar parameters from Southworth & Evans 2016) a substellar radius 10.5% larger than the planet's polar radius. More detailed simulations of the effect of tidal distortion on transmission spectra are however beyond the scope of this work.

As demonstrated by Deming & Sheppard (2017), observations at low to medium spectral resolution are affected by an resolution linked bias (RLB), which acts to decrease the apparent absorption feature amplitude. This is due to flux leakage from neighboring spectral regions into the absorption line, where the planetary atmosphere's enhanced absorption is located. We have evaluated the RLB affecting our measurements of the Na and K lines following the formalism of Deming & Sheppard (2017) (Eqs. (3)–(5)), and assuming an instrumental spectral resolution of 1200 together with our smallest bin size of 2 nm. We find that the effect is small compared to our uncertainties, 2.0×10^{-4}, 5.4×10^{-5}, and 2.9×10^{-5} in $\Delta R_p/R_*$ for the 2 nm bins centered on the Na and the blue and red components of the K feature, respectively.

4.4. Atmospheric metallicity and cloud altitude

We compare our data to model atmospheres calculated for metallicities 0.1, 1 and 10 times the solar value. The data are most closely reproduced by models with super-solar metal abundances, evidenced by χ^2 values of 51.1, 56.0 and 60.0 when comparing data to models of 10, 1, and 0.1 solar metallicity. This is due to slightly enhanced absorption measured at wavelengths larger than 900 nm, where water absorption becomes prominent. Extending WASP-103's transmission spectrum to longer wavelengths, targeting prominent water absorption features, would be required to make a more solid statement on the planet's atmospheric composition. We show the predicted transmission spectra in the near-IR in the right panel of Fig. 7, indicating the location of HST's WFC3 G141 grism, and precision estimate of 50 ppm (e.g., Kreidberg et al. 2015). Water should be easily detectable in the atmosphere of WASP-103b.

We do not observe any evidence for aerosols in the planetary transmission spectrum. This means that, if clouds or hazes are present in the atmosphere of WASP-103b, they must be located at altitudes below (or pressure levels larger than) those probed by our measurements. For the models calculated here, the atmospheric pressure levels probed outside the alkali features range between 0.01 bar (for 10 × solar metallicity) and 0.1 bar (for 0.1 × solar metallicity). If a cloud deck is present in the atmosphere of WASP-103b, it must reside at pressures higher than 0.01 bar. This upper limit is well inside the range of inferred cloud deck altitudes for hot Jupiters (e.g., Barstow et al. 2017).

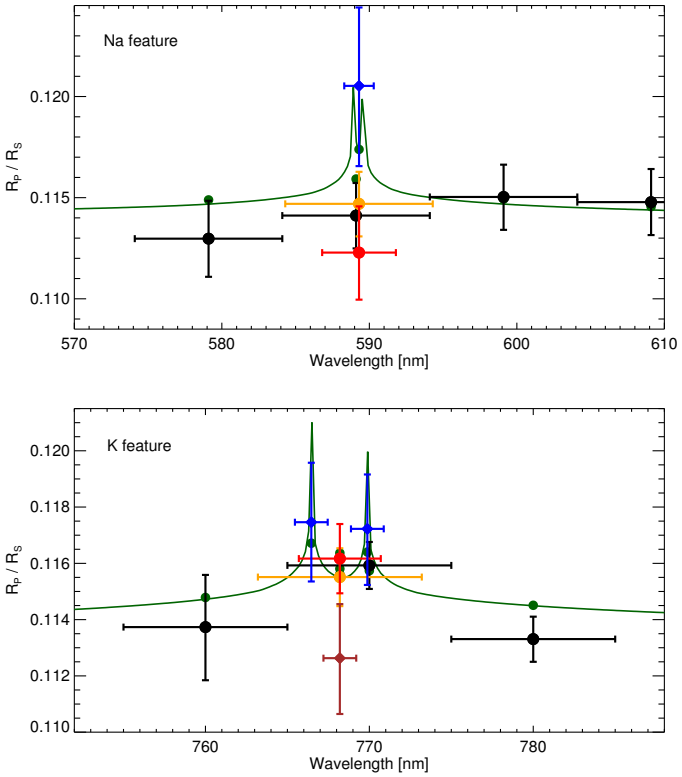


Fig. 8. Transmission spectrum of WASP-103b zoomed in on the Na (*top*) and K (*bottom*) features. The black points refer to the 10 nm wavelength bins also shown in Fig. 6, blue points indicate 2 nm bins centered on the features: either one bin centered on the Na feature, or two point centered on each component of the K feature. In the *lower panel*, brown refers to a 2 nm wide bin centered between the two components. Red and orange points denote wavelength bins of 5 and 10 nm width, respectively, centered on the features. The solar-composition model spectrum is shown in green, and filled circles indicate the model binned to the resolution of the data.

4.5. The atmosphere of WASP-103b in context

Based on these measurements, we tentatively classify WASP-103b as a planet with a clear atmosphere. The absence of a wavelength-dependent slope in our data, combined with the detection of alkali absorption indicates that aerosols, if present in substantial quantities in the atmosphere of WASP-103b, exist largely at altitudes below those probed by tranmsission spectroscopy. The planet follows the trends of Stevenson (2016), who proposed that hot planets, and planets with high surface gravities, are more likely to possess large water absorption features expected from clear atmospheres. Along the same lines, the planet also follows the cloudiness-temperature relation proposed by Heng (2016), who find that alkali absorption features are most pronounced for hot planets.

In terms of mass and temperature, WASP-103b greatly resembles WASP-12b, an object for which a detailed transmission spectrum has been observed (Mandell et al. 2013; Sing et al. 2013; Swain et al. 2013; Stevenson et al. 2014; Kreidberg et al. 2015). At the precision of the available data, the optical transmission spectrum of WASP-12b does not show alkali absorption features, however it does show a wavelength-dependent slope, which can be interpreted as signs of an aerosol layer (Sing et al. 2013; Barstow et al. 2017). Water has been detected (Kreidberg et al. 2015) in near-IR observations, but also these observations are best fit when including an additional atmospheric opacity source. It appears thus that the spectrum of WASP-12b is more strongly affected by clouds or hazes than that of WASP-103b. However, direct comparison between results for the two planets is not straight-forward as our observations of WASP-103b have a different resolution and wavelength coverage than those by (Sing et al. 2013) of WASP-12b. Our data have a higher spectral resolution, and we are thus more sensitive to absorption in the alkali line cores, which may have gone undetected for WASP-12b. At the same time, our data cover a more narrow wavelength-region and are thus less sensitive to scattering slopes. Based on our detection of alkali features in the optical part of the spectrum, we would expect WASP-103b to show also a prominent water feature in its near-IR transmission spectrum. Near-IR observations, but also observations spanning a wider wavelength region in the optical will allow a more detailed characterization of WASP-103b's atmosphere. Also, higher-resolution optical observations of WASP-12b would be an asset to make the available data on these two planets truly comparable.

5. Conclusions

We present an optical transmission spectrum of the highly irradiated exoplanet WASP-103b using Gemini/GMOS covering the wavelength range between 550 and 960 nm. WASP-103b is one of the closest-orbiting hot Jupiters known, with an equilibrium temperature of 2500 K and an orbital separation of less than 1.2 times the Roche limit. From a combined analysis of observations from three individual transits, we find enhanced absorption at the 589 nm Na and, at lesser significance, at the 766 nm K feature. This indicates that the transmission spectrum of WASP-103b is not dominated by strong aerosol absorption, a finding that is in line with previously-published trends of aerosol appearance and planetary properties (Heng 2016; Stevenson 2016). Based on the altitudes probed by our data, we constrain the pressure at the top of any potential clouds in the atmosphere of WASP-103 to be at least 0.01 bar. At low significance, the Na feature as well as both components of the K feature, show slightly enhanced absorptions compared to predictions from a solar-composition planetary atmosphere model.

Our observations do not confirm a previously-inferred strong trend for increasing absorption at small wavelengths (Southworth et al. 2015; Southworth & Evans 2016). We have studied the impact of contamination from a blended star on the transmission spectrum, but fail to produce a trend large enough to explain previous observations even when assuming errors on the stellar parameters of both stars at the 3-σ level.

Acknowledgements. We thank an anonymous referee for insightful comments that improved the quality of this work. We acknowledge Laetitia Delrez and Catherine Huitson for valuable discussions on the treatment of contamination and the wavelength stability of GMOS. I.J. acknowledgements support from the Austrian Research Promotion Agency (FFG) under grant number P847963. Based on observations obtained at the Gemini Observatory, which is operated by the Association of Universities for Research in Astronomy, Inc., under a cooperative agreement with the NSF on behalf of the Gemini partnership: the National Science Foundation (United States), the National Research Council (Canada), CONICYT (Chile), Ministerio de Ciencia, Tecnología e Innovación Productiva (Argentina), and Ministério da Ciência, Tecnologia e Inovação (Brazil).

References

Barstow, J. K., Aigrain, S., Irwin, P. G. J., & Sing, D. K. 2017, ApJ, 834, 50
Blecic, J. 2016, Ph. D. Dissertation [arXiv:1604.02692]
Blecic, J., Harrington, J., & Bowman, M. O. 2016, ApJS, 225, 4
Borysow, A. 2002, A&A, 390, 779

Borysow, A., & Frommhold, L. 1989, ApJ, 341, 549
Borysow, J., Frommhold, L., & Birnbaum, G. 1988, ApJ, 326, 509
Borysow, A., Frommhold, L., & Moraldi, M. 1989, ApJ, 336, 495
Borysow, A., Jorgensen, U. G., & Fu, Y. 2001, J. Quant. Spectr. Rad. Transf., 68, 235
Budaj, J. 2011, AJ, 141, 59
Burrows, A., Marley, M. S., & Sharp, C. M. 2000, ApJ, 531, 438
Carlin, B., & Louis, T. 2009, Bayesian methods for data analysis, Texts in statistical science (CRC Press)
Cartier, K. M. S., Beatty, T. G., Zhao, M., et al. 2017, AJ, 153, 34
Charbonneau, D., Brown, T. M., Noyes, R. W., & Gilliland, R. L. 2002, ApJ, 568, 377
Chen, G., Palle, E., Nortmann, L., et al. 2017, A&A, 600, L11
Cubillos, P. E. 2016, Ph. Dissertation [arXiv:1604.01320]
Cubillos, P., Harrington, J., Loredo, T. J., et al. 2017, AJ, 153, 3
Deming, D., & Sheppard, K. 2017, ApJ, 841, L3
Deming, D., Wilkins, A., McCullough, P., et al. 2013, ApJ, 774, 95
Espinoza, N., & Jordán, A. 2015, MNRAS, 450, 1879
Gelman, A., & Rubin, D. 1992, Statist. Sci., 7, 457
Gillon, M., Lanotte, A. A., Barman, T., et al. 2010, A&A, 511, A3
Gillon, M., Anderson, D. R., Collier-Cameron, A., et al. 2014, A&A, 562, L3
Heng, K. 2016, ApJ, 826, L16
Holman, M. J., Winn, J. N., Latham, D. W., et al. 2006, ApJ, 652, 1715
Husser, T.-O., Wende-von Berg, S., Dreizler, S., et al. 2013, A&A, 553, A6
Kausch, W., Noll, S., Smette, A., et al. 2015, A&A, 576, A78
Kreidberg, L., Line, M. R., Bean, J. L., et al. 2015, ApJ, 814, 66
Lammer, H., Selsis, F., Ribas, I., et al. 2003, ApJ, 598, L121
Lecavelier Des Etangs, A., Pont, F., Vidal-Madjar, A., & Sing, D. 2008a, A&A, 481, L83
Lecavelier Des Etangs, A., Vidal-Madjar, A., Désert, J.-M., & Sing, D. 2008b, A&A, 485, 865
Leconte, J., Lai, D., & Chabrier, G. 2011, A&A, 528, A41
Lendl, M., Delrez, L., Gillon, M., et al. 2016, A&A, 587, A67
Mandel, K., & Agol, E. 2002, ApJ, 580, L171
Mandell, A., Haynes, K., Sinukoff, E., et al. 2013, ApJ, 779, 128
Matsumura, S., Peale, S. J., & Rasio, F. A. 2010, ApJ, 725, 1995
Ngo, H., Knutson, H. A., Hinkley, S., et al. 2016, ApJ, 827, 8
Nikolov, N., Sing, D. K., Gibson, N. P., et al. 2016, ApJ, 832, 191
Patra, K. C., Winn, J. N., Holman, M. J., et al. 2017, AJ, 154, 4
Pont, F., Tamuz, O., Udalski, A., et al. 2008, A&A, 487, 749
Rothman, L. S., Gordon, I. E., Barber, R. J., et al. 2010, J. Quant. Spectr. Rad. Transf., 111, 2139
Schwarz. 1978, Ann. Stat., 6, 461
Sedaghati, E., Boffin, H. M. J., Jeřabková, T., et al. 2016, A&A, 596, A47
Sing, D. K., Lecavelier des Etangs, A., Fortney, J. J., et al. 2013, MNRAS, 436, 2956
Sing, D. K., Wakeford, H. R., Showman, A. P., et al. 2015, MNRAS, 446, 2428
Sing, D. K., Fortney, J. J., Nikolov, N., et al. 2016, Nature, 529, 59
Smette, A., Sana, H., Noll, S., et al. 2015, A&A, 576, A77
Southworth, J., & Evans, D. F. 2016, MNRAS, 463, 37
Southworth, J., Mancini, L., Ciceri, S., et al. 2015, MNRAS, 447, 711
Stevenson, K. B. 2016, ApJ, 817, L16
Stevenson, K. B., Bean, J. L., Seifahrt, A., et al. 2014, AJ, 147, 161
Swain, M., Deroo, P., Tinetti, G., et al. 2013, Icarus, 225, 432
ter Braak, C. J. F. T. 2006, Statistics and Computing, 16, 239
ter Braak, C. J. F., & Vrugt, J. A. 2008, Statistics and Computing, 18, 435
Udry, S., Mayor, M., & Santos, N. C. 2003, A&A, 407, 369
van Dokkum, P. G. 2001, PASP, 113, 1420
Vidal-Madjar, A., Lecavelier des Etangs, A., Désert, J.-M., et al. 2003, Nature, 422, 143
von Essen, C., Cellone, S., Mallonn, M., et al. 2017, A&A, 603, A20
Winn, J. N., Holman, M. J., Torres, G., et al. 2008, ApJ, 683, 1076
Wöllert, M., & Brandner, W. 2015, A&A, 579, A129

Appendix A: Additional tables

Table A.1. Wavelength bins, contamination flux ratios ($F_{\rm cont}/F_{W103}$) for WASP-103 and the nearby source, and quadratic limb-darkening coefficients used in the analysis.

Wavlength range [nm]	$F_{\rm cont}/F_{W103}$	u_1	u_2	Wavelength range [nm]	$F_{\rm cont}/F_{W103}$	u_1	u_2
10 nm bins				20 nm bins			
554.1–564.1	0.047 ± 0.0099	0.499	0.208	554.1–574.1	0.049 ± 0.0098	0.493	0.209
564.1–574.1	0.051 ± 0.0098	0.488	0.210	574.1–594.1	0.051 ± 0.0099	0.472	0.212
574.1–584.1	0.053 ± 0.0097	0.477	0.211	594.1–614.1	0.056 ± 0.0097	0.450	0.217
584.1–594.1	0.049 ± 0.0103	0.466	0.213	614.1–634.1	0.056 ± 0.0100	0.432	0.219
594.1–604.1	0.055 ± 0.0099	0.459	0.212	634.1–654.1	0.060 ± 0.0097	0.399	0.232
604.1–614.1	0.056 ± 0.0095	0.449	0.214	654.1–668.9	0.065 ± 0.0094	0.383	0.235
614.1–624.1	0.056 ± 0.0101	0.436	0.218	673.0–689.6	0.063 ± 0.0108	0.383	0.226
624.1–634.1	0.057 ± 0.0100	0.429	0.218	695.0–715.0	0.067 ± 0.0095	0.366	0.197
634.1–644.1	0.059 ± 0.0100	0.426	0.187	715.0–735.0	0.070 ± 0.0089	0.350	0.199
644.1–654.1	0.061 ± 0.0094	0.398	0.201	735.0–755.0	0.073 ± 0.0080	0.350	0.213
654.1–664.1	0.065 ± 0.0093	0.384	0.236	755.0–775.0	0.075 ± 0.0082	0.339	0.214
664.1–668.9	0.064 ± 0.0096	0.393	0.227	775.0–795.0	0.077 ± 0.0080	0.318	0.232
673.0–681.3	0.063 ± 0.0106	0.387	0.226	795.0–812.2	0.079 ± 0.0074	0.308	0.234
681.3–689.6	0.062 ± 0.0112	0.381	0.226	816.0–832.8	0.081 ± 0.0072	0.292	0.236
695.0–705.0	0.066 ± 0.0094	0.371	0.227	838.3–858.3	0.083 ± 0.0072	0.276	0.242
705.0–715.0	0.067 ± 0.0097	0.361	0.198	858.3–878.3	0.086 ± 0.0070	0.278	0.237
715.0–725.0	0.069 ± 0.0094	0.354	0.198	878.3–898.3	0.087 ± 0.0070	0.279	0.232
725.0–735.0	0.071 ± 0.0085	0.350	0.230	898.3–918.3	0.089 ± 0.0067	0.275	0.231
735.0–745.0	0.072 ± 0.0081	0.343	0.230	918.3–938.3	0.091 ± 0.0062	0.273	0.228
745.0–755.0	0.073 ± 0.0080	0.347	0.213	938.3–957.8	0.093 ± 0.0061	0.261	0.232
755.0–765.0	0.075 ± 0.0078	0.348	0.206				
765.0–775.0	0.075 ± 0.0084	0.331	0.225	Na feature			
775.0–785.0	0.077 ± 0.0082	0.320	0.232	584.3–594.3	0.049 ± 0.010	0.465	0.215
785.0–795.0	0.078 ± 0.0077	0.314	0.233	586.8–591.8	0.044 ± 0.011	0.479	0.200
795.0–805.0	0.079 ± 0.0075	0.314	0.224	588.3–590.3	0.032 ± 0.010	0.466	0.214
805.0–812.2	0.079 ± 0.0073	0.310	0.225				
816.0–824.4	0.080 ± 0.0073	0.296	0.236	K feature			
824.4–832.8	0.082 ± 0.0072	0.288	0.239	763.2–773.2	0.075 ± 0.0084	0.328	0.230
838.3–848.3	0.083 ± 0.0073	0.281	0.234	765.7–770.7	0.074 ± 0.0085	0.329	0.220
848.3–858.3	0.084 ± 0.0072	0.280	0.234	767.2–769.2	0.076 ± 0.0084	0.325	0.231
858.3–868.3	0.086 ± 0.0070	0.270	0.241	765.46–767.46	0.072 ± 0.0084	0.327	0.232
868.3–878.3	0.086 ± 0.0071	0.273	0.236	768.88–770.8.8	0.074 ± 0.0086	0.326	0.232
878.3–888.3	0.087 ± 0.0069	0.268	0.239				
888.3–898.3	0.088 ± 0.0070	0.265	0.240	white			
898.3–908.3	0.090 ± 0.0069	0.280	0.225	5541–9578	0.069 ± 0.0087	0.341	0.226
908.3–918.3	0.089 ± 0.0066	0.279	0.223				
918.3–928.3	0.092 ± 0.0062	0.275	0.225				
928.3–938.3	0.091 ± 0.0064	0.273	0.223				
938.3–948.3	0.092 ± 0.0061	0.265	0.207				
948.3–957.8	0.095 ± 0.0061	0.254	0.212				

Table A.2. Transmission spectrum of WASP-103b as observed with GMOS.

Wavlength range [Å]	$(\Delta R_p/R_*)_i$	Wavelength range [Å]	$(\Delta R_p/R_*)_i$
10 nm bins		20 nm bins	
5541–5641	−0.0035 ± 0.0024	5541–5741	−0.00356 ± −0.0014
5641–5741	−0.0024 ± 0.0019	5741–5941	−0.00137 ± −0.0012
5741–5841	−0.0014 ± 0.0019	5941–6141	0.00029 ± −0.0012
5841–5941	−0.0003 ± 0.0016	6141–6341	0.00299 ± −0.0010
5941–6041	0.0006 ± 0.0016	6341–6541	−0.00161 ± −0.00087
6041–6141	0.0004 ± 0.0016	6541–6689	−0.00334 ± −0.00097
6141–6241	0.0024 ± 0.0012	6730–6896	−0.00259 ± −0.00099
6241–6341	0.0035 ± 0.0013	6950–7150	−0.00101 ± −0.00080
6341–6441	−0.0009 ± 0.0012	7150–7350	0.00124 ± −0.00068
6441–6541	−0.0019 ± 0.0012	7350–7550	0.00047 ± −0.00066
6541–6641	−0.0049 ± 0.0012	7550–7750	0.00087 ± −0.00095
6641–6689	−0.0007 ± 0.0015	7750–7950	−0.00140 ± −0.00057
6730–6813	−0.0028 ± 0.0012	7950–8122	−0.00051 ± −0.00080
6813–6896	−0.0024 ± 0.0012	8160–8328	−0.00192 ± −0.00088
6950–7050	−0.0021 ± 0.0012	8383–8583	−0.00064 ± −0.00082
7050–7150	0.00008 ± 0.00086	8583–8783	0.00033 ± −0.00083
7150–7250	0.00195 ± 0.00095	8783–8983	−0.0003 ± −0.0010
7250–7350	0.00086 ± 0.00088	8983–9183	0.00018 ± −0.00083
7350–7450	−0.00009 ± 0.00090	9183–9383	0.0005 ± −0.0012
7450–7550	0.00081 ± 0.00088	9383–9578	0.0004 ± −0.0013
7550–7650	−0.0007 ± 0.0019		
7650–7750	0.00151 ± 0.00083	Na feature	
7750–7850	−0.00111 ± 0.00080	5843–5943	0.0003 ± −0.0016
7850–7950	−0.00146 ± 0.00089	5868–5918	−0.0021 ± −0.0023
7950–8050	0.0010 ± 0.0011	5883–5903	0.0061 ± −0.0039
8050–8122	−0.0019 ± 0.0012		
8160–8244	−0.0023 ± 0.0010	K feature	
8244–8328	−0.0016 ± 0.0013	7632–7732	0.0011 ± −0.0010
8383–8483	0.0012 ± 0.0010	7657–7707	0.0018 ± −0.0012
8483–8583	−0.00316 ± 0.00098	7672–7692	−0.0018 ± −0.0020
8583–8683	0.0012 ± 0.0010	7654.6–7674.6	0.0030 ± −0.0021
8683–8783	0.0005 ± 0.0012	7688.8–7708.8	0.0028 ± −0.0020
8783–8883	0.0014 ± 0.0014		
8883–8983	−0.0014 ± 0.0011		
8983–9083	−0.0003 ± 0.0012		
9083–9183	−0.0008 ± 0.0015		
9183–9283	0.0000 ± 0.0015		
9283–9383	0.0019 ± 0.0022		
9383–9483	−0.0011 ± 0.0018		
9483–9578	0.0035 ± 0.0021		